

State Localization and Selective Charge Filtering Near a Null Point

Sanjoy Patra,[†] Jibin Sivanarayan,[‡] Vivek N. Bhat,[†] Philip D. Maret,[‡] Atandrita Bhattacharyya,[†] Sayan Ghosh,[†] Mahesh Hariharan,^{*,‡} and Vivek Tiwari^{*,†}

[†]*Solid State and Structural Chemistry Unit, Indian Institute of Science, Bangalore, Karnataka 560012, India*

[‡]*School of Chemistry, Indian Institute of Science Education and Research, Thiruvananthapuram, Kerala 695551, India.*

E-mail: mahesh@iisertvm.ac.in; vivektiwari@iisc.ac.in

Abstract

Null points in synthetically tunable molecular aggregates are predicted to generate flat energy bands analogous to those known in strongly correlated condensed-matter physics. For chemistry, null points provide a powerful design principle for photovoltaic materials with selective charge filtering similar to photosynthesis. However, null points have never been experimentally verified because their defining prediction – state localization with selective electron or hole transfer – has remained unobserved. Here, using a donor–acceptor dyad as a minimal model, we provide the first experimental observation of a null point. Impulsive pump–probe measurements reveal charge separation through a near-instantaneously generated locally excited–charge transfer (LE–CT) intermediate that emerges upon solvent stabilization of CT states. Polarization anisotropy directly reveals state localization and selective charge-filtering, spanning balanced electron–hole transfer to selective hole filtering consistent with synthetic design. A generalized vi-

tronic theory of null points explains these observations and identifies the ideal synthetic parameters for achieving null points which are protected from the vibrational bath.

Introduction

Photosynthetic reaction center proteins¹ are pigment-protein complexes which can separate charge across tens of angstroms to create a microsecond long charge-separated state with near-unity quantum efficiency. The mechanism for the fastest steps of this process is now understood^{2,3} to proceed through admixtures of vibrational-electronic (vibronic) states. This efficient design has inspired synthetically tunable molecular aggregates where a similarly fast charge separation, transport and eventual stabilization into a charge-separated state with low recombination probability is desirable. Such molecular constructs, which achieve charge separation between identical chromophores are termed as symmetry-breaking charge separation^{4,5} (SB-CS) systems, and may find potential applications as the active layer in organic photovoltaics.

π -stacked molecular aggregates form locally excited (LE) Frenkel exciton type states as well as charge-transfer (CT) states due to orbital overlaps. Interference between long-range Coulomb (J_C) and CT couplings results in the rich landscape of non-Kasha^{6,7} molecular aggregates. Using a purely electronic description, Spano and co-workers have predicted that such interference can also lead to flat energy bands, termed as null points,⁸ thus opening the possibility of synthetically tunable molecular materials with strongly correlated excitons similar to layered materials with flat energy bands⁹ known in condensed matter physics. For photochemistry, Spano has shown that null points are exceptionally susceptible⁸ to solvent induced energetic fluctuations, leading to SB-CS with selective hole or electron transfer. Charge filtering and simultaneous suppression, through destructive interference between orbitals, of undesirable photophysical pathways which can arise in strongly coupled aggregates

makes null points quite a versatile design in the broad context of fine tuning molecular photophysics towards desirable photoproducts. For example, selective charge filtering property with suppressed charge recombination channels finds promise as electron and hole transporting layers in photovoltaic applications. However, coupling to the vibrational bath, particularly at room temperature, can readily disrupt the intended functionality of null points, and remains an open question.

The electronic description of Spano and co-workers also predicts⁶ null excitons where, weak $LE - CT$ mixing through electron and hole overlap integrals, t_e and t_h , respectively, can be treated perturbatively such that J_{CT} and J_C interfere destructively. Spectroscopically, this phenomenon should result in monomer-like absorption spectrum of the aggregate. Indeed, several recent experimental demonstrations of null excitons,¹⁰⁻¹⁶ based on approximate resemblance of the linear absorption spectrum to that of the monomer, have generated significant interest in the particular context of SB-CS.

Null points are a more general concept and should be distinguished from null excitons. The presence of null excitons does not imply the existence of null points. The latter arise from band degeneracies and have yet to be experimentally verified. As elucidated by Spano,⁸ the former arises only in the perturbative limit of CT coupling, whereas the latter constitutes a broader regime that enables selective charge filtering through state localization. To date, experimental evidence for null excitons relies primarily on the approximate similarity of linear absorption spectra to that of the monomer. In contrast, state localization with selective charge filtering—the key predicted signature of a null point—has not been experimentally realized. Verifying this prediction, and understanding the dynamical behavior of excitons in a vibrational bath near a null point, is the focus of this work.

The existence of null points and the resulting charge asymmetry is expected to be highly

sensitive⁸ to the perturbations to CT energies, fluctuations in the solvation environment, and the molecular geometry changes in going from a crystal environment, where the molecular geometry is characterized, to a solvated environment. Furthermore, vibronic couplings, so far not considered in the electronic description of null points, can interfere¹⁷ and delocalize^{18,19} electronic states. Whether selective charge filtering at null points intended by synthetic design even translates into the corresponding quantum dynamics is a question that remains unaddressed. Mechanistic questions such as the effect of linear vibronic couplings on the predicted orbital interference, and whether linear optical spectra adequately report on null excitons are all hard to decipher based on spectroscopic observables such as ratio of Franck-Condon (FC) intensities in the linear spectra, fluorescence lifetimes and non-impulsive PP experiments.

$D - A$ systems, in combination with impulsive optical probes and polarization-control, provide a model template for establishing mechanistic connections between the intended synthetic design and the dynamical behavior of excitons near null points. Deviating from all previous synthetic designs which rely on the destructive interference between finite J_C and J_{CT} couplings with balanced or comparable t_e and t_h couplings, we recently reported¹⁴ a Greek-cross architecture perylenediimide (PDI) donor-acceptor ($D - A$) dyad where J_C is suppressed by relative geometry and J_{CT} is suppressed because of strongly imbalanced electron and hole overlap integrals, that is, $t_h \gg t_e$. The photophysics in polar solvents showed SB-CS in as fast as 627 fs with unprecedented charge separation to recombination rate ratio of 2947 inferred through a combination of linear spectra, fluorescence lifetime and non-impulsive pump-probe (PP) measurements. Following Spano's terminology⁸ for lopsided electron and hole transfer integrals, we refer here to the more specific parameter regime of suppressed dipolar couplings together with strongly imbalanced t_e and t_h orbital overlaps as the lopsided regime. As our analysis will show, suppressed dipolar couplings are essential for protecting state localization near the null point against vibronic delocalization couplings.

Recent impulsive PP experiments^{10,20} on PDI based null exciton dimers and trimers report ultrafast charge separation through coherently excited intermediates with *CT* character. However, as noted earlier, null points in SB-CS systems have never been experimentally realized. In this context, polarization control has provided unprecedented insights into ultrafast vibronic phenomenon such as in tracking electronic reorientation through a Jahn-Teller conical intersection.^{21,22} Here we present sub-10 fs temporal resolution, polarization-controlled, two-color PP experiments to provide the first experimental verification of null points in the Greek-cross PDI dyads. In polar solvents, tetrahydrofuran (THF) and acetonitrile (ACN), we find evidence for a near-instantaneously photoexcited *LE* – *CT* intermediate state that subsequently evolves to a relaxed *CT* state. Polarization anisotropy directly tracks electronic reorientation during charge separation and confirms the predicted state localization and charge asymmetry expected near null points. We find that selective charge filtering behavior is strongly influenced by the solvent polarity – THF shows no such selectivity, whereas ACN, with significantly more *LE* – *CT* mixing, shows selective hole filtering as intended by synthetic design. A generalized vibronic description of null points confirm the presence of mixed *LE* – *CT* states and predicts a competing effect between electronic couplings conferred by synthetic design and linear vibronic couplings due to the intramolecular vibrational bath – the former causes desired electronic localization leading to selective charge filtering whereas the latter can delocalize electronic states and prevent the process. Our model predicts that the dominating influence of the solvation environment and the competing effect from linear vibronic couplings can be simultaneously minimized in the lopsided regime – significant imbalance between HOMO-HOMO versus LUMO-LUMO interference, and suppressed Coulomb interactions between the sites – as is the case for the Greek-cross PDI dyad. Our work provides the first experimental validation of null points and guides synthetic design towards null points that are protected from the vibrational bath.

Linear optical spectra show solvent polarity dependent deviations from the null exciton

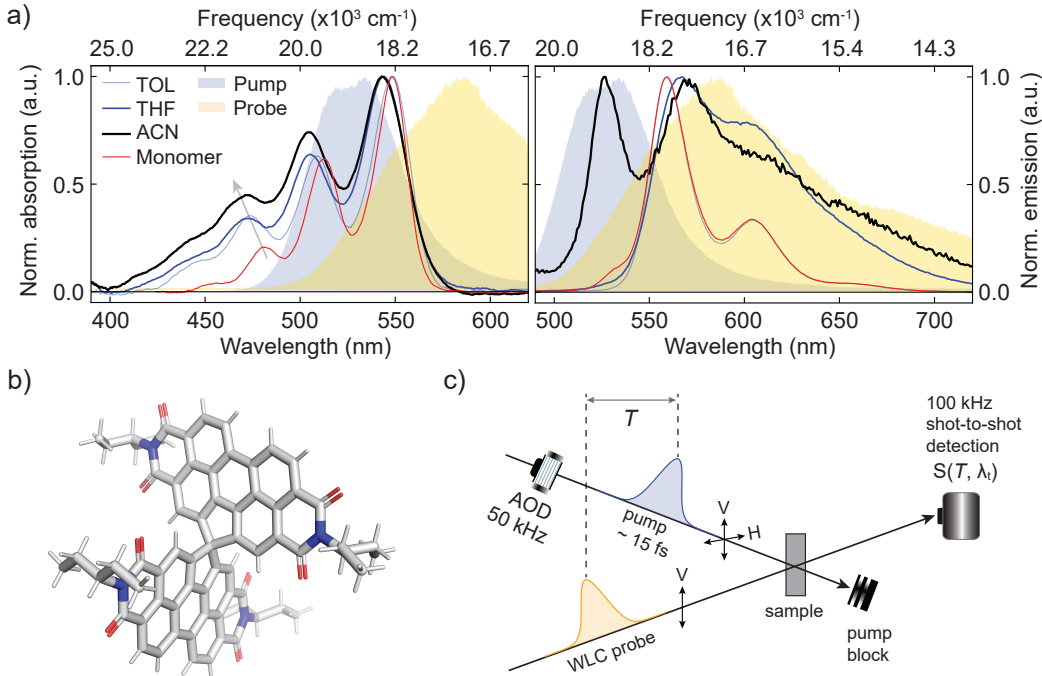


Figure 1: **Linear spectra of the Greek-cross spiro-conjugated PDI dimer (SpPDI2) and two-color polarization-controlled impulsive pump-probe (PP) setup.** (a) The absorption (left) and emission (right) spectrum of SpPDI2 in toluene (TOL), tetrahydrofuran (THF), and acetonitrile (ACN). The 24 nm red-shifted spectrum of the PDI monomer in TOL is also overlaid. The white light continuum (WLC) generated pump spectrum is blue shaded and centered at 525 nm. The WLC probe spectrum is gray shaded. (b) The Greek-cross (+) geometry of the SpPDI2 dimer obtained from the X-ray crystallographic structure¹⁴ is also shown for reference. (c) Schematic of the two-color PP (2C-PP) 100 kHz spectrometer. Polarization control on the pump and probe lines is denoted by vertical and horizontal arrows. T denotes the PP delay time. Full optical layout is shown in Figure S1a.

Figure 1a shows the solvent polarity dependent linear spectra of the SpPDI2 dimer. Solvent polarity increases from lower in TOL (dielectric constant $\epsilon = 2.38$) to THF ($\epsilon = 7.58$) to highest in ACN ($\epsilon = 37$). The fluorescence quantum yield¹⁴ reduces with increased polarity – from >90% in TOL to 24% in THF and <1% in ACN. Our previous work¹⁴ reported a mutual transition dipole angle of $\theta_{AB} = 87.4^\circ$ obtained through single-crystal X-ray structure. The determined Greek-cross geometry is shown in Figure 1b. Dipole angle dependent electronic structure calculations, described briefly in Section S3, show suppressed Coulomb coupling due to relative geometry despite only $\sim 3\text{-}4 \text{ \AA}$ separation between the PDI

chromophores, and constructive and destructive interference between HOMO-HOMO and LUMO-LUMO orbitals, respectively. This results in the lopsided regime, that is, minimal J_C and $t_h \gg t_e$. This architecture also satisfies the electronic criterion for lower-exciton band null point, $J_{ct_e t_h} > 0$ outlined by Spano.⁸ Note that this is a purely electronic criterion and is generalized in this work to account for the differences in stabilization energies, quenching of electronic couplings and vibrational-electronic couplings that can arise for vibronic excitons.

When the red-shifted PDI monomer spectrum in TOL is overlaid with the SpPDI2 dimer in TOL, close agreement between the I_{00}/I_{01} vibronic band intensities is seen, as previously reported¹⁴ – 1.74 for monomer versus 1.60 for the dimer. Assuming a large energy gap between the *CT* and *LE* states that justifies a second-order perturbative treatment⁶ of *LE-CT* couplings, destructive interference between J_C and J_{CT} , can indeed lead to a null exciton with monomer like peak intensities. All studies so far confirm null exciton formation through peak intensities in the linear optical spectra. However, subtle differences in peak intensities, such as those seen in the I_{02} and higher bands, hold vital clues regarding the sensitivity of null points to solvent polarity dependent variations in *LE-CT* mixing and the consequent changes in state localization near null points. With increase in polarity, deviations from the monomer absorption intensities, most notably under the higher vibronic progressions are increasingly evident. The corresponding emission spectrum (Figure 1, right) shows strong deviations from the monomer spectrum suggesting that relaxation pathways away from the Franck-Condon (FC) geometry are significantly modified even if J_C and J_{CT} destructively interfere. The lower lying emission peak in ACN was also confirmed by conducting the emission measurements at 400 nM concentrations where the intermolecular distance was greater than the Förster critical radius²³ of 17 Å for energy transfer and minimizes fluorescence re-absorption effects. This is shown in Figure S1. Figure 1c shows the polarization-controlled, 100 kHz shot-to-shot detected, two-color PP (2C-PP) setup where pump and probe white-light spectra are generated by focusing a $\sim 1 \mu\text{m}$ 1040 nm fundamental light into respective

YAG crystals. The white-light spectra are overlaid with the absorption and emission spectra in Figure 1a. Further details of the method are presented in Section S1 and described in our previous works.^{24,25} The two-color nature of the experiment implies dominant excitation of only the main absorption band, while the probe spectrum is centered on the emission lineshape to dominantly probe the excited state dynamics. In a two-dimensional electronic spectroscopy experiment, this corresponds to probing the lower cross-peak region. The pump pulse duration was measured to be ~ 15 fs obtained by maximizing two-photon intensity autocorrelation (Figure S1). The instrument response function obtained from a global fit across the >200 nm probe bandwidth is 35 fs (Figure S1).

Solvent polarity dependent, near-instantaneous generation of a [$LE + CT$] intermediate

Figure 2a shows the early PP waiting time (T) PP spectra for the three solvents. A strong positive band resulting from the overlapping ground state bleach (GSB) and stimulated emission (SE) signals is seen for all cases. However the SE band shoulder persistent in TOL at 605 nm vanishes within ~ 250 fs for both THF and ACN cases, and leads to the formation of cation and anion bands near 580 nm and 730 nm, marked by red and blue vertical lines, respectively. The loss of SE signal is consistent with the reduced fluorescence quantum yield with solvent polarity. Our previous report¹⁴ with slow instrument response confirmed the presence of cation and anion bands beyond 1 ps. These were found to be consistent with the PDI monomer cation and anion bands (see Figure S18 of ref.¹⁴). With the impulsive 2C-PP experiments, a global fit and target analysis of the PP dataset in Figure 2b shows species associated spectra (SAS) of an intermediate species with mixed LE and CT spectral features. The corresponding decay associated spectra (DAS) are shown in Figure S2. Similar to recent reports^{10,20} of coherently photoexcited intermediates in SB-CS, we assign this intermediate to a near-instantaneously generated mixed [$LE + CT$] intermediate. The near-instantaneous

generation is confirmed by the corresponding concentration profiles in Figure 2c which show that 37 % of the intermediate concentration is already present at the singlet maxima. Figure S5 overlays the PP spectra for early delay times to show the generation of the intermediate within the instrument response of ~ 35 fs. The intermediate concentration maximizes with time constants of ~ 150 fs and ~ 180 fs for THF and ACN, respectively, and subsequently evolves to a relaxed CT state on a 2.95 ps and 0.62 ps timescale for THF and ACN, respectively. The above picture is schematically represented in the right panel of Figure 2c. The cation and anion bands, marked in Figure 2b, also show increased amplitude with increasing solvent polarity from THF to ACN. Note that, as shown in Figure S2, the same global model when applied to TOL leads to unphysical DAS with $<1-2\%$ amplitude contributions. Consequently, the resulting SAS for the initially excited and the relaxed S_1 species in Figure 2b(top) show nearly identical spectra with no indication of a $[LE + CT]$ intermediate in the case of TOL.

Similar coherently photoexcited $[LE+CT]$ intermediates in SB-CS have been recently^{10,20} reported to mediate SB-CS in PDI based systems. The accompanying vibrational quantum beats were reported to promote relaxation toward a relaxed CT state away from the FC geometry. We find an absence of vibrational quantum beats during the impulsive generation of the $[LE+CT]$ and its subsequent relaxation to the CT state. Figures S6-S9 show that in a related chiral PDI dimer²⁶ (CyPDI2) in which no null points are expected based on Coulomb couplings, and electron and hole transfer integrals are not imbalanced (Section S3), the same PP spectrometer and data analysis pipeline shows absence of $[LE + CT]$ intermediate. Compare Figure S5 for SpPDI2 with Figure S6 for the CyPDI2 dimer. However, the SB-CS process in the CyPDI2 dimer is accompanied by prominent vibrational quantum beats in the range of $\sim 100-1600$ cm^{-1} (Figure S7). These results are summarized in Section S2. We note that several previous works²⁷⁻²⁹ show that spectator quantum beats, which have isotropic polarization signatures,³⁰⁻³² can simply accompany internal conversion or be excited by it,

and do not report on a functional role for such nuclear motions.

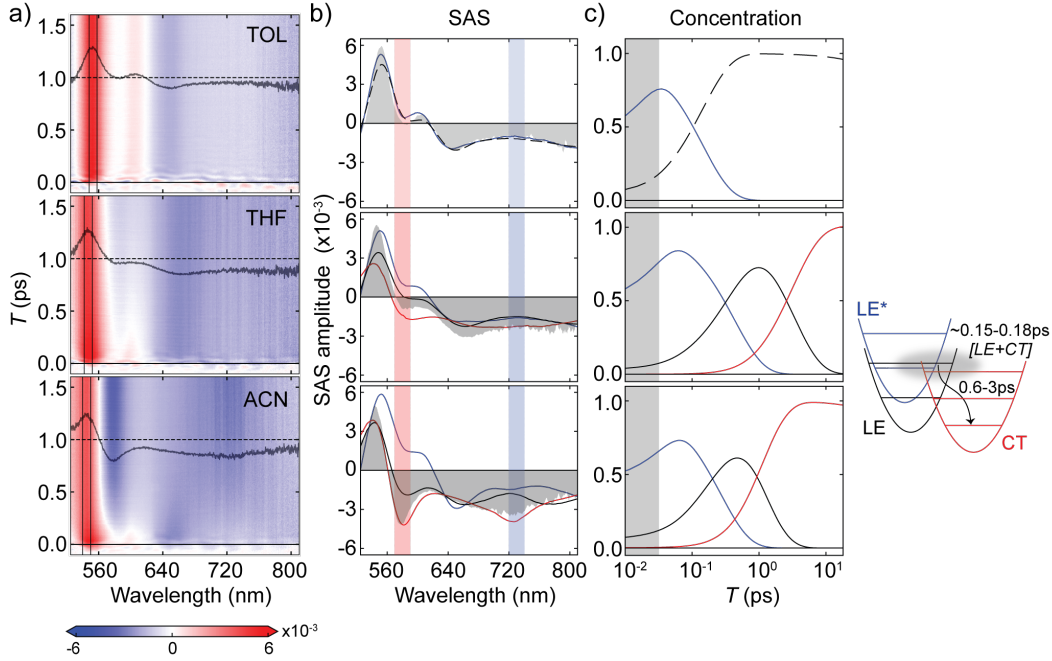


Figure 2: Solvent-polarity dependent near-instantaneous generation of $[LE+CT]$ intermediate. (a) Early time magic angle PP spectra for TOL (top), THF (middle) and ACN (bottom). The black trace in the contour plot represents the PP spectrum at $T = 1$ ps. The full PP spectra and time constants obtained after global fitting are shown in Figure S2. (b) Species associated spectra (SAS) derived from the global fit. The cation and anion bands are denoted by red and blue bands respectively. The gray shaded area represents the PP spectrum at $T = 1$ ps. (c) The corresponding concentrations. The gray band at 35 fs marks the 1-99 % rise of the instrument response. The target model for the SAS analysis is shown on the right. The intermediate corresponds to a near-instantaneously photoexcited $[LE + CT]$ intermediate with a timescale of ~ 150 fs and ~ 180 fs for THF and ACN respectively. The relaxation of this intermediate to the CT state occurs on the timescale of 0.62 ps and 2.97 ps for THF and ACN respectively.

Electronic anisotropy reports state localization and selective hole transfer

Two strongly coupled and isoenergetic and electronically coupled LE sites $|A\rangle$ and $|B\rangle$ form perfectly mixed excitons $(|A\rangle \pm |B\rangle)/\sqrt{2}$ where we denote⁸ the phase of the linear combination by a subscript on the wave vector k , as $|k_0^{LE}\rangle$ and $|k_\pi^{LE}\rangle$, respectively. In case of large spectral overlaps, such electronic mixing may not produce spectral changes during T . In such situations, polarization anisotropy can serve as a sensitive probe of electronic dynamics. Solvent polarity dependent $[LE + CT]$ intermediate formation and the expected

null point behavior in this system prompted us to use polarization anisotropy to directly track the transition dipole reorientation that accompanies these steps. During internal conversion between the LE and CT states, the expected change in the electronic anisotropy³³ is $r(\theta_{ij}) = \frac{(3\cos^2(\theta_{ij})-1)}{5}$, where i, j are the transition dipole directions corresponding to the initial and final probed species. For instance, for orthogonally polarized i, j transitions, electronic anisotropy of approximately -0.2 has been recently reported³⁴ by Vauthey and co-workers in the context of $CT D-A$ dyad. In case of the SB-CS dimer studied here, species i is the initially excited LE state while j could be the intermediate or the relaxed CT species formed later. Note that a simple consideration as above does not account for impulsive excitation, shared ground state electronic correlations between the sites, and $LE-CT$ couplings as expected in the SpPDI2 dimer. Later in this section, we account for these effects to formulate a generalized anisotropy model starting from a CT dimer Hamiltonian and simulate the resulting electronic anisotropy near null points.

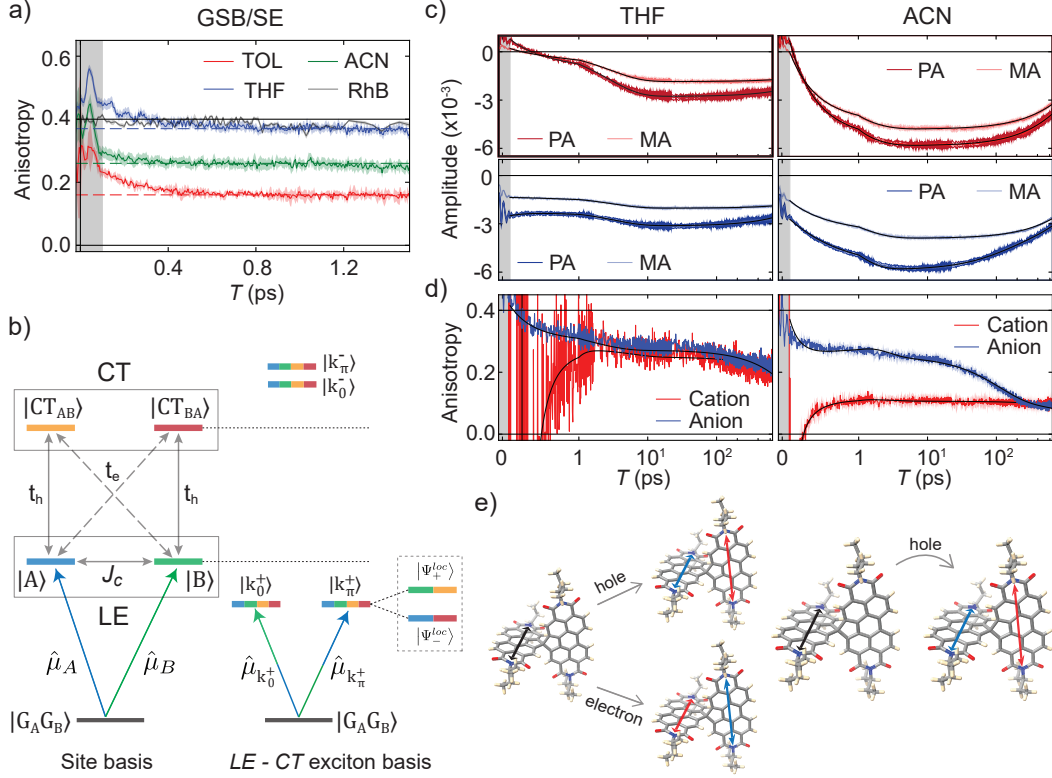


Figure 3: Electronic anisotropy reports state localization and selective hole transfer expected near null points. Electronic anisotropy in the (a) GSB/SE band for solvents of varying polarity. The corresponding PP transients are shown in Figures S2 and S4. The reference electronic anisotropy of 0.4 for a single $S_0 \rightarrow S_1$ transition dipole is marked by a horizontal line and experimentally measured to be 0.381 ± 0.086 in the $T = 100\text{-}200$ fs window for Rhodamine B (RhB) in ethanol (Figure S3). The other horizontal lines denote the settling value of the anisotropy of SpPDI2 in different solvents which is determined by averaging the 1–2 ps time window (Table S2). The error bar is obtained by averaging 3 trials and shown as $\pm\sigma/\sqrt{N}$ band on the average. The anisotropy in the first 100 fs region, where the coherent artifacts persist in the corresponding PP transients (Figure 2a), is grayed out. (b) A purely electronic CT dimer model⁸ in the diabatic site basis qualitatively explains the observed anisotropy trends as arising from state localization and selective hole filtering near the null point. $G_A G_B$ denotes the initially shared ground state between the sites. A, B denote the collective LE states where only one of the sites is electronically excited. The LE states are mutually coupled through long-range dipole couplings J_C . The CT states couple to the LE states through electron and hole overlap integrals, t_e and t_h , respectively. The dashed box shows that starting from a LE – CT (delocalized) exciton basis, the resulting states vectors show state localization⁸ and selective hole transfer at the null point. The electronic character is represented by color and the full analytic derivation is presented in Section S4. (c) PP transients in the cation (top) and anion (bottom) bands for the case of THF and ACN. (d) The corresponding electronic anisotropy. The corresponding PA and MA fits are shown in thin black lines and the anisotropy fit is derived from these fit functions (Table S2). (e) Illustration of cation (red) and anion (blue) transition dipole alignments³⁵ involved in non-selective (left) versus selective (right) hole transfer.

Figure 3 plots the electronic anisotropy derived from the PP data in Figure 2. The GSB/SE band and the cation and anion bands are marked in Figure 2. Electronic polarization anisotropy can be derived³³ from PP experiments conducted with any two of the

parallel (PA), perpendicular (PE) and magic angle (MA) relative pump and probe polarizations. In our case, the anisotropy is derived from the PA and MA polarization sequence as $r(T) = (S_{PA} - S_{MA})/2S_{MA}$, where S is the PP signal in any given spectral band. The anisotropy plots shown in Figure 3a are averaged over three trials. The corresponding full PP transients for the GSB/SE band are plotted in Figure S2 and S4 and the settling anisotropy in the 1-2 ps time window is summarized in Table S2. Using the same polarization optics, the reference anisotropy of 0.381 ± 0.086 between $T = 100$ -200 fs obtained for Rhodamine B (RhB) in ethanol, close to 0.4 expected from an isolated transition dipole, is shown in Figure S3. Full T range anisotropy of RhB is shown in Figure S3 with anisotropy of 0.004 ± 0.001 at $T = 600$ ps. In case of SpPDI2 in TOL, where no $[LE + CT]$ intermediate was observed in Figure 2a, the early T anisotropy in the GSB/SE band undergoes an initial drop that is attributable to excited state electronic relaxation and settles at 0.160 ± 0.014 by ~ 600 fs. Jonas and co-workers have shown³⁶ that the GSB electronic anisotropy (r_{GSB}) of excitonic dimers and square symmetric molecules with orthogonally polarized transition dipoles is 0.1 with isotropic signal strength of $S_{MA}^{GSB} = 2S_{MA}^{SE}$, because shared ground state implies that bleach on one molecules also affects the other. Similarly, r_{SE} is expected to be 0.4 after all electronic coherences are dephased and assuming no further excited state electronic reorientation. The resulting total expected anisotropy in the GSB/SE band, $r_{tot} = (S_{MA}^{GSB}r_{GSB} + S_{MA}^{SE}r_{SE})/(S_{MA}^{GSB} + S_{MA}^{SE})$ becomes 0.2 for a purely excitonic dimer in reasonable agreement to that seen for TOL. Contamination from the ESA signal overlapping with the GSB/SE band is likely to be minor contributing factor in the reduced anisotropy. In order to estimate whether oscillator strength borrowed by energetically higher lying CT states through $LE - CT$ mixing affects the expected anisotropy, in Section S5 we extend the purely excitonic dimer description to a CT dimer and analytically show that the observed anisotropy is insensitive to $LE - CT$ mixing. Therefore, the purely excitonic description qualitatively explains the reduced GSB/SE anisotropy for SpPDI2 in TOL as dominantly arising from a shared ground state.

An immediately interesting aspect of this result is that the SpPDI2 dimer, even in the case of TOL where I_{00} and I_{01} relative intensities are similar to those in the monomer (Figure 1) and no $[LE + CT]$ intermediate is observed, is not a null exciton with monomer like optical properties – the observed anisotropy reveals a shared ground state and significant electronic delocalization between the sites (Figure 4a). To the best of our knowledge, so far the existence of a null exciton has been based on comparisons of linear absorption intensities in the I_{00} and I_{01} bands. Our results for TOL – electronic anisotropy and simulated linear vibronic spectra in Figure 4a – demonstrate that deviations from monomer vibronic intensities in the I_{02} and higher bands and the electronic anisotropy subtly report on non-negligible effects such as $LE - CT$ mixing and electronic delocalization between the sites, respectively, which are precluded under the assumption of perturbative CT couplings.

Compared to TOL, the presence of an $[LE + CT]$ intermediate in THF and ACN cases suggests stabilization of CT states with increasing solvent polarity. Curiously, the settling GSB/SE anisotropy rises to 0.370 ± 0.014 in case of THF. The same rising trend in GSB/SE anisotropy is also seen for the case of ACN which shows even greater amplitude of the $LE - CT$ intermediate (Figure 2b,c) and settles at 0.258 ± 0.017 . Spano has illustrated⁸ how fluctuations in the solvation environment lead to state localization near null points due to mixing between the excitons of different phase. For instance, as illustrated in Figure 3b and analytically shown in Section S4 for a model with $t_h \gg t_e$ as for the SpPDI2 dimer, transforming a CT dimer model to a $LE - CT$ exciton basis shows the mixing between the LE and CT excitons. The resulting $LE - CT$ excitons in the lower energy band are degenerate and denoted as $|k_0^+\rangle$ and $|k_\pi^+\rangle$, where $+$ denotes the phase of the linear combination. Solvent induced energetic fluctuations mixes them to result in a localized state with only $|B\rangle$ optically bright character with no electronic delocalization between the A and B sites (see Section S4.1 for full derivation). This is illustrated in Figure 3b where the color

tracks electronic character. In such a localized state with no shared ground state electronic correlations between the two sites, the resulting anisotropy will increase towards the isolated transition dipole limit of 0.4. This idea is illustrated in Figure S15 which calculates the electronic anisotropy at the exact null point with state localization versus away from it where the delocalized sites A and B share a common ground state. Therefore, solvent fluctuation driven state localization near null points explains the increased anisotropy in case of THF and ACN. The SE signal contribution, with its anisotropy of 0.4, is only expected in case of THF – quantum yield $\phi = 24\%$ in THF versus $<1\%$ in case of ACN – and qualitatively explains the higher GSB/SE anisotropy in case of THF versus ACN. Note that our first guess for increased r_{tot} in THF and ACN compared to TOL was the increased $LE - CT$ mixing suggested by simulations of linear vibronic intensities (Figure 4a). This expectation³⁷ is valid for excitonic dimers where borrowing of oscillator strength by higher lying states not covered by the laser spectrum, increases r_{GSB} towards 0.4, the isolated transition dipole limit. However, our calculations in Section S5, both analytic and numerical, show that r_{GSB} for the lower exciton band of the CT dimer remains at ~ 0.1 despite $\sim 50\%$ $LE - CT$ mixing. Eqn. S23 and Figure S14 in Section S5 show that the insensitivity of r_{GSB} is specific to the lopsided parameter regime – $t_h \gg t_e$ and suppressed J_C . Thus, our hypothesis of a lack of shared ground state due to state localization near null points, outlined in Figure S15, is most consistent with the observed anisotropy trends.

As illustrated in Figure 3b, the key verification of a null point is whether state localization, inferred here through polarization anisotropy in the GSB/SE band, is also accompanied by selective hole filtering given that the hole transfer integral t_h is synthetically engineered to be significantly larger than the electron transfer integral t_e ? Figure 3c shows the PA and MA transients in the cation and anion bands for the case of THF and ACN solvents. The corresponding electronic anisotropy is shown in Figure 3d. For the case of THF, the anion band shows larger anisotropy initially. However, this anisotropy is only maintained until ~ 1

ps, beyond which both bands show overlaying anisotropy as the $[LE + CT]$ intermediate relaxes to a CT state. In contrast, the ACN case, which shows more prominent spectral signatures of the $[LE + CT]$ intermediate (Figure 2b), behaves exactly as synthetically engineered – the anion band anisotropy is significantly larger than the cation band with both merging on the timescales of molecular rotation. Following the argument³⁵ of Vauthey and co-workers, Figure 3e illustrates that the observed anisotropic charge transfer is a direct consequence of selective hole transfer, that leads to the localized state $|B\rangle - |CT_{AB}\rangle$ (Section S4 and Figure 3b). A larger anisotropy is seen in the anion band because the initial LE transition dipole on a given site, say $\hat{\mu}_B$, and the final transition dipole on the anionic site that contributes to the ESA transition, $\hat{\mu}_{B \rightarrow B^*}$, are parallel.³⁸

We have also conducted experiments on a chiral CyPDI2 dimer²⁶ (Section S2), where electronic structure calculations (Section S3 and Figure S9) do not predict null points. The predicted absence of a null point in CyPDI2 is attributable to the lack of imbalance between t_e and t_h resulting from only partial HOMO-HOMO constructive and LUMO-LUMO destructive orbital interference. This essential difference between the SpPDI2 and CyPDI2 dimers is illustrated in Figure S9c,d. Experimentally SB-CS is observed in CyPDI2 but without any evidence for a $[LE + CT]$ intermediate (Figure S6). In contrast to SpPDI2, no signatures of state localization are observed in the GSB/SE anisotropy (Figure S6e), and the cation and anion band anisotropies do not report any anisotropic charge transfer (Figure S8b). Along similar lines, earlier work³⁵ by Vauthey et al. on a perylene dyad without synthetically engineered null points also reported no intermediates or anisotropic charge transfer during SB-CS.

Interestingly our observations show that synthetic design for null points and the solvation environment, both strongly influence the directionality of charge transfer – non-selective on longer timescales in THF to selective hole filtering, as intended by synthetic design, in ACN. To understand these observations better, next we simulate the solvent-dependent vibronic

intensities for the SpPDI2 dimer.

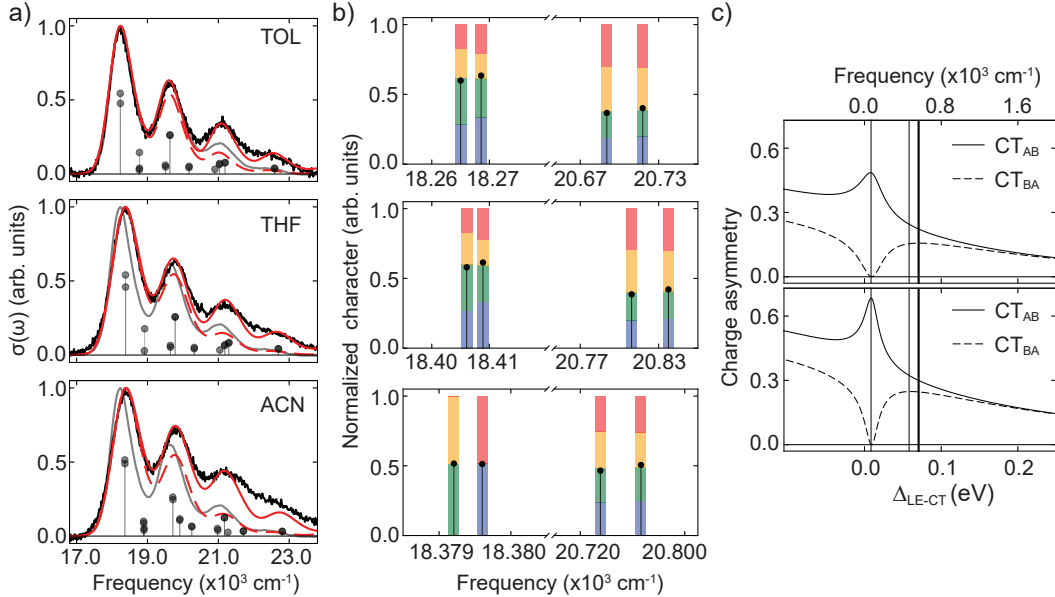


Figure 4: Vibronic CT dimer model connects solvent polarity dependent anisotropic charge transfer to null points. (a) Simulated absorption spectrum for TOL (top), THF (middle) and ACN (bottom). Solid lines show the experimental spectrum of the dimer (black) and the 24 nm red-shifted monomer (gray). The dashed red curve is the absorption spectrum simulated without any $LE-CT$ mixing. The red curve corresponds to the optimized $\Delta_{LE-CT} = E_{CT} - E_{LE}$ energy gap which captures the increased absorption intensities under the higher vibronic shoulders. The corresponding stick spectra, without the Brownian oscillator lineshapes, are also shown for this case. (b) The corresponding purely electronic oscillator strengths along with state characters. The state characters for ACN are the same as in Figure 3b. (c) Charge asymmetry and null points in the purely electronic (top) and the vibronic (bottom) dimer models corresponding to the case of ACN. Energetic fluctuations at the null point induced by the solvent are fixed at $\delta E = 10^{-4}$ eV. The three vertical lines correspond to the Δ_{LE-CT} energy gap that describes the optimized absorption intensities in panel a. The parameters are described in Table S4.

Vibronic description of null points connects solvent polarity dependent anisotropic charge transfer to linear spectra

The electronic CT dimer model starts from the diabatic site basis states – $|G_A G_B\rangle$ for the shared ground state, $|A\rangle$ and $|B\rangle$ for the locally excited states, and $|CT_{AB}\rangle$ and $|CT_{BA}\rangle$ for the CT states $|A^+ B^-\rangle$ and $|A^- B^+\rangle$, respectively. The electronic Hamiltonian in the site basis, \hat{H}_{elec}^{site} is shown in Eqn. S1. The general analytic derivation of the resulting electronic eigenstates for any J_C , t_e and t_h electronic couplings, including the lopsided parameter

regime for the SpPDI2 dimer, is presented in Section S4. The resulting localized states at null points, caused by an energy fluctuation δE induced by the solvent, are illustrated in Figure 3b. Extending this picture to a vibronic description, we include a high- and a low-frequency intramolecular vibrational mode explicitly in the system Hamiltonian to fully account for rich effects such as electronic delocalization caused by vibronic mixing,^{18,39} interference of vibronic couplings along low- and high-frequency vibrations^{10,20,30} and their interplay with CT couplings within a numerically exact basis set description without any N-particle approximation.¹⁸ Linear vibronic couplings from the rest of the intramolecular vibrational bath are treated as Brownian oscillators, and impart broadened lineshapes to the absorption sticks in Figure 4a. Calculations for electronic couplings – J_C , t_e and t_h follow our earlier report¹⁴ on the SpPDI2 dimer and described in Section S3. All the model parameters are summarized in Table S3 and S4. It should be emphasized that only the $LE - CT$ energy gap, $\Delta_{LE-CT} = E_{CT} - E_{LE}$, is floated to account for the solvent polarity dependent stabilization of the CT states. All other parameters derived from electronic structure calculations are kept fixed across the solvents. The resulting vibronic intensities are plotted in Figure 4a and compared with the dimer (black) and monomer (gray) absorption spectra.

As noted earlier in the discussion of Figure 1, the deviations in the I_{01} and higher vibronic shoulders compared to the monomer follow the solvent polarity. Simulations of vibronic intensities in Figure 4a show that the observed trends in the absorption intensities are explained by the largest $LE - CT$ mixing in case of ACN due to stabilized CT states in the polar solvent (compare the dashed versus solid red curves in Figure 4a). For THF and TOL, the CT states are progressively less stabilized such that $LE - CT$ mixing is reduced and so are the corresponding vibronic intensities under I_{02} and higher energy shoulders. The corresponding electronic state characters are plotted in Figure 4b. With increasing solvent polarity, and therefore increasing $LE - CT$ mixing, the color-coded electronic characters show maximum state localization for the case of the ACN solvent. The localized state characters plotted in

Figure 3b correspond to the electronic null point in Figure 4b.

To further visualize⁸ state localization, which should result only in CT_{AB} or CT_{BA} character, Figure 4c(top) plots the corresponding CT character of the lowest exciton of the purely electronic model as a function of Δ_{LE-CT} . Larger $LE-CT$ mixing through reduced Δ_{LE-CT} also ensures proximity to the null point and consequently maximum charge asymmetry and selectivity in hole transfer. The Δ_{LE-CT} values estimated by fitting the vibronic intensities for the three solvent cases are indicated by the vertical lines in Figure 4a. When $LE-CT$ mixing is less such as in the case of THF and TOL solvents, deviations in $> I_{02}$ vibronic intensities compared to the monomer are also lesser. At the same time, the system is farther away from the null point. Consequently, the charge asymmetry is lesser such that both electron and hole transfer become equally probable as reported by the equal cation and anion band anisotropies for the case of THF.

Overall, by relating absorption intensity trends to increased $LE-CT$ mixing, the calculations in Figure 4 elucidate the influence of solvent polarity on state localization and selective hole transfer near null points. We note that our theoretical model only qualitatively explains our experimental observations – solvent polarity dependent vibronic shoulder intensities (Figure 1), and state localization with anisotropic charge transfer (Figure 3). This is so because the optimized fits to the linear spectra are tolerant to $\pm 10-20\%$ variations in the estimated Δ_{LE-CT} gaps, and to $\sim 10\times$ variations in the already suppressed J_C Coulomb coupling (Figure S13). Such variations in the estimated parameters are well within the estimation error⁴⁰ from electronic structure calculations across different basis sets and in the presence of a solvent.

Lopsided parameter regime protects null points from the vibrational bath

The above observations naturally raise the question of how – if at all – electronic null points are modified by coupling to the vibrational bath. In Section S4.2, we develop a vibronic framework for describing null points that elucidates the role of linear vibronic coupling in either stabilizing or suppressing them. This analysis further identifies the parameter regimes in which null points remain protected against the vibrational bath.

The derivations in Section S4 generalize the vibronic exciton framework^{30,41,42} to *CT* dimers and only the key points regarding the modification of null points due to vibronic couplings are briefly described below. Denoting the numerically exact vibronic basis states as $|A\rangle|0_B\rangle \prod_{j \in \{H,L\}} |\tilde{v}_j^A\rangle |v_j^B\rangle$, where *H*, *L* correspond to the high and low frequency intramolecular vibrational modes in the system Hamiltonian, and \tilde{v} denotes the FC displaced vibrational basis states on the electronically excited site, *A* in this case. As detailed in Section S4 and illustrated in Figure 3b, transformation from site basis to the *LE* – *CT* exciton basis leads to eigenvectors $|k_\pi^+\rangle$ and $|k_0^+\rangle$ in the lower energy band. As shown in Eqn. S7 and Eqn. S10, a solvent induced energetic fluctuation δE couples the two states with coupling matrix element $\delta E \sin \theta_1 \sin \theta_2 \prod_{j \in \{H,L\}} \langle \tilde{v}_j^A | v_j^A \rangle \langle v_j^B | \tilde{v}_j^B \rangle$, where θ_1 and θ_2 are electronic mixing angles (Eqn. S3) between *LE* and *CT* states which depend only on J_C , t_e , t_h and Δ_{LE-CT} . The vibrational overlap factors, such as $\langle \tilde{v}_j^A | v_j^A \rangle$ between $|A\rangle$ and $|0_A\rangle$ partly quench the electronic coupling through δE . However, as seen from Eqn. S15 and Table S5, the FC displacements of the $U_{|k_\pi^+\rangle}$ and $U_{|k_0^+\rangle}$ diabatic exciton potentials are approximately equal in the lopsided regime. This is illustrated in Figure S12 where no relative FC displacement is seen between them. This imposes a vibrational selection rule whereby state localization due to a fluctuation δE occurs predominantly without any change in vibrational quanta. We will term this coupling due to δE as ‘localization coupling’.

Similar vibrational overlap factors indeed partially quench all the electronic couplings to modify the null point. For example, J_C is quenched by vibrational overlap factors $\prod_{j \in \{H,L\}} \langle \tilde{\nu}_j^A | \nu_j^A \rangle \langle \nu_j^B | \tilde{\nu}_j^B \rangle$ (Eqn. S10). Additionally, vibrational stabilization energy on each excitonic state also modifies the null point degeneracy as $E_{k_0^+} - E_{k_\pi^+} = \Delta \lambda_{k_0^+ - k_\pi^+}$ (Eqn. S16) where the right hand side is the difference between the total vibrational stabilization energy λ associated with $U_{|k_\pi^+}$ and $U_{|k_0^+}$ diabatic exciton potentials. However, suppressed J_C and the lack of relative FC displacements between the $U_{|k_\pi^+}$ and $U_{|k_0^+}$ potentials in the lopsided regime (Figure S12), ensure that the null point degeneracy condition is not affected. The minor effects from linear vibronic couplings are seen in Figure 4c (bottom) where for the vibronic CT dimer model, the width of charge asymmetry η (Eqn. S19) due to δE fluctuation is only partly reduced, and to have the null point degeneracy at the same Δ_{LE-CT} as the purely electronic case (top), only a minor modification of J_C , from 15.5 cm^{-1} to 20.3 cm^{-1} , is required. Overall, the influence of linear vibronic couplings on the null point, mediated by intramolecular vibrational motions, is strongly suppressed in the lopsided parameter regime.

Low-frequency vibrations can inhibit state localization at null points

In the context of excitonic dimers, linear vibronic couplings are also well understood to promote electronic delocalization^{39,43} at vibronic resonances, where excitation of vibrational quanta can compensate for energetic mismatch between states. In terms of state mixing, imperfectly mixed electronic character is enhanced to near-perfect mixing at a vibronic resonance. For example, see the red curve in Figure 4 of ref.¹⁸ which quantifies electronic mixing by an inverse participation ratio. The effect of linear vibronic couplings is best seen when the vibrational part of the Hamiltonian, \hat{H}_{LVC} in Eqn. S9, is written in terms of correlated and anti-correlated vibrational coordinates,⁴⁴ \hat{q}_{j+} and \hat{q}_{j-} , respectively (Eqns. S11-S12), where the latter is akin to the tuning coordinate in conical intersections.⁴⁵ In the $LE - CT$ exciton basis, \hat{H}_{LVC} transforms to couple the $U_{|k_\pi^+}$ and $U_{|k_0^+}$ potentials through coupling elements

$-(\omega_j^2 S_j)^{1/2}(\hat{q}_{j-} \cos \theta_1 \cos \theta_2)$ (Eqns. S13-S14), where S_j is the Huang-Rhys factor along the j^{th} intramolecular vibrational coordinate.

As noted earlier, the diabatic exciton potentials $U_{|k_{\pi}^{\pm}\rangle}$ and $U_{|k_0^{\pm}\rangle}$ exhibit no relative FC displacement (Figure S12). Consequently, vibronic couplings along \hat{q}_{j-} (Eqn. S13) involve transitions with $\Delta v = \pm 1$, whereas localization couplings are dominant for $\Delta v = 0$, i.e., in the absence of changes in vibrational quanta. A change in vibrational quanta along the tuning coordinate \hat{q}_{j-} couples $U_{|k_{\pi}^{\pm}\rangle}$ and $U_{|k_0^{\pm}\rangle}$ diabatic exciton potentials away from a null point when they are not degenerate. This coupling delocalizes the electronic character and therefore has the opposite effect of δE localization couplings. We term it as delocalization coupling. The competing nature of both couplings – localization coupling due to solvent induced δE fluctuations and delocalization coupling due to vibronic resonances – are summarized in Figure 5a. Note that as seen in Eqn. S14, the \hat{q}_{j+} coordinate is akin to the seam space in conical intersections and does not participate in mixing the $LE - CT$ excitons.

It is important to emphasize that the exclusivity and selectivity of localization and delocalization coupling channels – arising via $\Delta v = 0$ and $\Delta v = \pm 1$, respectively – are direct consequences of the lopsided parameter regime. In this regime, the null point degeneracy is not only protected against quenching of electronic couplings and vibrational stabilization, but the competing delocalization arising from vibronic couplings is relegated to a distinct channel, separate from the desired δE induced localization.

Just like δE localization couplings which impart a width to a null point (Figure 4c), resonant vibronic couplings also have a width proportional to $\sqrt{S_j} \cos \theta_1 \cos \theta_2$, that is, to the strength of vibronic coupling along a given coordinate and electronic mixing angles between the LE and CT excitons (Eqn. S3). Thus, for low-frequency vibrations and environmental modes,⁴¹ which can tune energy gaps between A and B sites, null point resonance which

causes electronic localization and vibronic resonance which causes electronic delocalization can overlap for a range of Δ_{LE-CT} energy gaps. The latter can compete against localization couplings to suppress state localization and charge asymmetry near the null point. This effect is illustrated in Figure 5b which plots charge asymmetry near a null point for a system with low-frequency vibrations. The low-frequency ($\sim 36 \text{ cm}^{-1}$) intramolecular vibrational mode couples the lower-energy $LE - CT$ excitons away from the null point. Owing to the finite width of this resonance and the associated electronic delocalization, state localization and the resulting charge asymmetry becomes increasingly confined to the immediate vicinity of the null point.

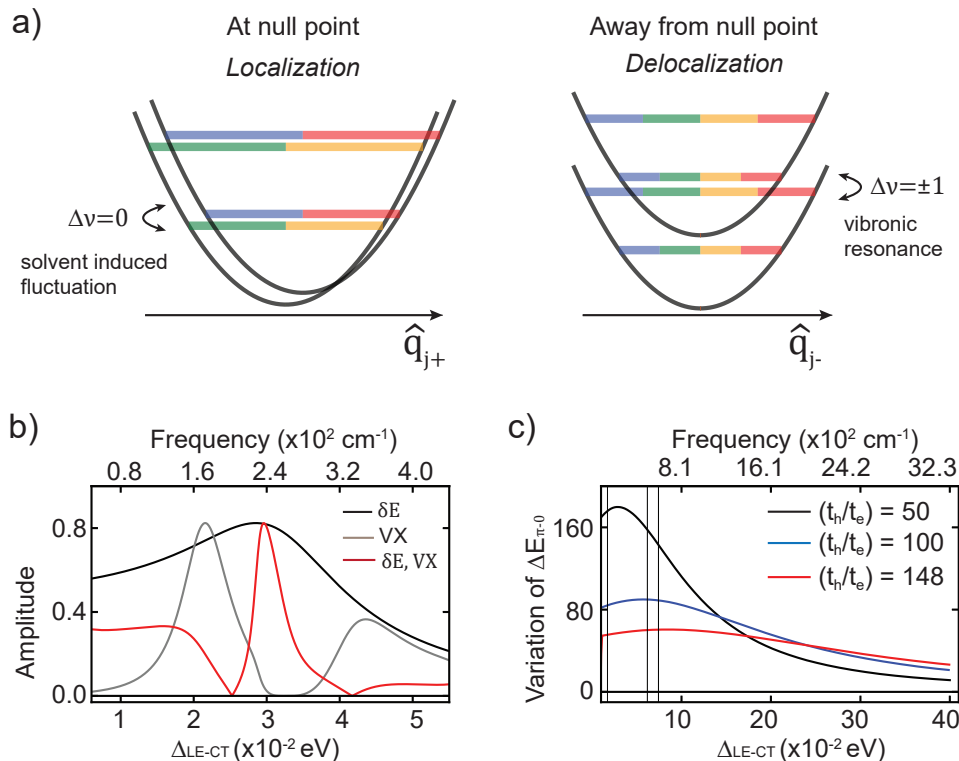


Figure 5: Low-frequency vibrations can inhibit null points (a) State localization due to solvent induced δE energetic fluctuations versus electronic delocalization due to vibronic resonances along low-frequency energy gap tuning modes \hat{q}_{L-} . The former occurs dominantly without any change in vibrational quantum number. The latter coupling channels delocalize the imperfectly mixed non-degenerate electronic states by compensating the energetic mismatch between the two $LE - CT$ excitons by a low-frequency vibrational quanta. In the lopsided regime the $\Delta v = 0$ and $\Delta v = \pm 1$ channels become exclusive. (b) Black curve plots the charge asymmetry versus Δ_{LE-CT} caused by a fluctuation δE , without any linear vibronic coupling in the system. State localization peaks at that Δ_{LE-CT} which leads to null point degeneracy, $\Delta E_{\pi-0} = |E_{k_q^+} - E_{k_\pi^+}| = 0$ and has a associated width. The gray curve, with δE absent but including the linear vibronic coupling shows the oscillator strengths of the upper exciton $|k_\pi^+\rangle$ near a vibronic resonance with a 36 cm^{-1} low-frequency mode, denoted as VX. The energetic mismatch $\Delta E_{\pi-0}$ is compensated by a low-frequency vibrational quantum, leading to intensity borrowing and enhanced oscillator strength near resonance. The red curve plots charge asymmetry when both δE and VX are present in the system. (c) Variation in $\Delta E_{\pi-0}$ with Δ_{LE-CT} , $\frac{\partial \Delta E_{\pi-0}}{\partial \Delta_{LE-CT}}$ plotted as a function of Δ_{LE-CT} for fixed J_C and t_e , same as in Figure 4, and different (t_h/t_e) ratios. The highest ratio corresponds to the SpPDI2 dimer. Further details of the calculations are presented in Section S4.3.

The analysis in Figure 5b suggests that low-frequency vibrations with large reorganization energies will compete against state localization electronic null points through vibronic resonances near null points. Large Huang-Rhys factors on low-frequency vibrations are not desirable because they ensure that such resonances are broad³⁰ such that exact resonances do not matter and even multiple⁴² low-frequency near-resonant modes can collectively suppress localization.

The next question is whether there exist synthetic parameters, analogous to the lopsided parameter regime, that render the energy gap $\Delta E_{\pi-0}$ between lower-band excitons insensitive to solvent-polarity-induced stabilization of CT states. Such a design can suppress competing delocalization couplings by lowering the cutoff beyond which low-frequency vibrational modes cannot achieve vibronic resonance with the near-zero $\Delta E_{\pi-0}$ at the null point. The ideal parameter regime must ensure minimal changes in $\Delta E_{\pi-0}$ with solvent induced variations in Δ_{LE-CT} . Using the analytic expression in Eqn. S5, the variation of $\Delta E_{\pi-0}$ with Δ_{LE-CT} , that is, $\frac{\partial \Delta E_{\pi-0}}{\partial \Delta_{LE-CT}}$ is plotted in Figure 5c for fixed values of J_C and t_e and varying (t_h/t_e) ratio. For a fixed J_C , least variation in $\Delta E_{\pi-0}$ is seen when $t_h \gg t_e$. Figure S11 shows a similar plot as Figure 5c but with a fixed lopsided (t_h/t_e) ratio and varying J_C . Again, variations in $\Delta E_{\pi-0}$ are minimal when dipolar couplings are suppressed as for the Greek-cross dimer studied here. These latter findings are consistent with those recently proposed by Spano.⁸ The analysis in Figure 5 implies that given a variation in the Δ_{LE-CT} gap created by the solvent, the corresponding variations around the null point, that is, in $\Delta E_{\pi-0} \sim 0$ will be least. This implies two things – 1.) The null point degeneracy in the lopsided regime is also the most robust to solvent polarity. And, 2.) the null point is only affected by the lowest frequency vibrations. Dynamically it also means that a slower vibrational mode will be less effective in causing electronic delocalization such that electronic localization can prevail sooner than delocalization.

Overall, our analysis shows that a combination of lopsided t_h and t_e couplings along with suppressed dipolar Coulomb couplings, as for the SpPDI2 dimer studied here, is most ideal to protect the null point – first, by minimizing the impact of local variations in solvation environments on the null point degeneracy, and second by minimizing the impact of intramolecular vibrations on the desirable state localization by creating exclusive coupling channels for localization versus delocalization couplings.

Conclusions

We provide the first experimental validation of a null point and predict the ideal synthetic regime to achieve the same. This is established through its hallmark signature—state localization with selective charge filtering. Polarization anisotropy is demonstrated as a sensitive probe of transition dipole reorientation, directly linking synthetic design to null point. We formulate a vibronic description of null points that captures the interplay of resonances and coupling interference, to enable direct connections with experimental observables. In particular, solvent-dependent vibronic intensities, state localization, and selective hole filtering are consistently explained by polarity-dependent $LE - CT$ mixing near the null point.

Our results also underscore the dominant role of the solvation environment while identifying the parameter regime that mitigates its influence. In particular, the lopsided parameter regime with suppressed dipolar couplings is predicted to optimally preserve null-point degeneracy and state localization by minimizing the competing effects of low-frequency vibrations and solvent polarity. Overall, this work establishes the key design criterion and optical signatures for future studies of engineered null points.

Methods

Two-color pump-probe and anisotropy experiments

Two-color white-light PP measurements were performed as described previously.^{24,25} A 1040 nm output from a Yb:KGW amplifier was split equally into pump and probe arms, each carrying about 1 μJ . The pump was modulated at 50 kHz, and pump/probe white-light continua were generated in 4 mm and 8 mm YAG crystals, respectively. Residual fundamental light was removed with shortpass filters, and dispersion in both arms was partially compensated with chirped mirrors. As shown in Figure S1, the pump pulse duration at the sample was ~ 15 fs, and the spectrally resolved PP data yielded an instrument response function of ~ 35 fs FWHM. Pump and probe were spatially overlapped and focused with an off-axis parabolic mirror to 70 μm $1/e^2$ spot diameters in a 200 μm cuvette at a crossing angle of $\sim 7.5^\circ$. Typical pulse energies at the

sample were 2.80 nJ (pump) and 1.24 nJ (probe). The delay was controlled with a motorized translation stage. Measurements were acquired in parallel and magic-angle polarization configurations. The polarization settings were verified using the procedures outlined previously³² and tested on Rhodamine B as a reference sample (Figure S3).

For rapid-scan experiments, the population time delay was scanned from -0.5 ps to 660 ps in four constant-velocity intervals. Global analysis of the PP data was performed in GloTarAn⁴⁶ and with custom Python scripts using multi-exponential kinetic models convolved with a Gaussian instrument response function. Data were chirp-corrected before fitting, and the DAS were extracted from the global fits. Target analysis was then used to test specific kinetic schemes and obtain SAS. Error bars were calculated from repeated parallel- and magic-angle measurements, and anisotropy uncertainties were propagated from the corresponding averaged transients.

Sample and Electronic Structure Calculations

Details of sample synthesis and characterization have been reported previously.^{14,26} SpPDI2 was dissolved in TOL, THF and ACN solvents to achieve the desired OD of 0.2-0.3 in 200 μ m cuvette. CyPDI2 exhibited very poor solubility in ACN rendering PP measurements in this solvent infeasible. All crystallographic computations were performed using the WINGX software suite. Three-dimensional molecular representations were generated using Mercury 3.10.1.4. Quantum chemical calculations were performed using Gaussian 16. Geometry optimizations were carried out at the DFT level employing the ω B97XD functional with the def2-SVP basis set in the gas phase unless otherwise specified. Vertical excitation energies and oscillator strengths were computed using time-dependent DFT (TD-DFT) at the same level of theory. Solvent-dependent TD-DFT calculations were conducted using the polarizable continuum model (PCM) with identical functional and basis set settings. Transition dipole moments for SpPDI2 were evaluated and visualized using Multiwfn 3.7.8 and VMD.

Vibronic Exciton Model and Calculations

The vibronic description of null points formulated in Section S4 extends the vibronic exciton framework of our previous works^{30,41,42} to *CT* dimers with *LE* and *CT* diabatic site states. A high- and a low-frequency intramolecular vibrational mode on each PDI chromophore are treated explicitly in the system Hamiltonian, without invoking the one-particle approximation,¹⁸ making the description numerically exact within the chosen basis. Each quantum oscillator has total 5 vibrational quanta which ensures convergence of $> I_{02}$ vibronic intensities. The parameters are listed in Table S4. For simulations of absorption intensities, the rest of the vibrational bath is modeled as Brownian oscillators (Table S3) which account for optical decoherence and impart broadening to the oscillator strength stick spectra. The height of vibronic shoulders in the linear spectra was tolerant to 10-20% changes in the Δ_{LE-CT} energy gap. Since J_C is suppressed to begin with, $10\times$ changes in J_C do not significantly affect vibronic intensities. The FC displacement d_{CT} on the *CT* states was found to be the most sensitive parameter that affects shoulder vibronic intensities and was optimized for the best fit (Figure S13). All the electronic parameters, except the Δ_{LE-CT} energy gap, are derived from the electronic structure calculations and kept fixed across the solvents. The vibrational parameters are derived from the fits to the PDI monomer lineshape (Figure S10) and the observed vibrational quantum beats (Figure S7).

Data Availability

The spectroscopic data generated in this study are available from the corresponding author upon a reasonable request.

Code Availability

Python scripts for data processing, analysis and vibronic exciton simulations are available from the corresponding author upon a reasonable request.

References

- (1) Blankenship, R. E. *Molecular Mechanisms of Photosynthesis*; Blackwell Science Ltd., 2002.
- (2) Policht, V. R.; Niedringhaus, A.; Willow, R.; Laible, P. D.; Bocian, D. F.; Kirmaier, C.; Holten, D.; Mančal, T.; Ogilvie, J. P. Hidden vibronic and excitonic structure and vibronic coherence transfer in the bacterial reaction center. *Science Advances* **2022**, *8*, eabk0953.
- (3) Paleček, D.; Edlund, P.; Westenhoff, S.; Zigmantas, D. Quantum coherence as a witness of vibronically hot energy transfer in bacterial reaction center. *Science Advances* **2017**, *3*, e1603141.
- (4) Sebastian, E.; Hariharan, M. Symmetry-Breaking Charge Separation in Molecular Constructs for Efficient Light Energy Conversion. *ACS Energy Letters* **2022**, *7*, 696–711.
- (5) Young, R. M.; Wasielewski, M. R. Mixed Electronic States in Molecular Dimers: Connecting Singlet Fission, Excimer Formation, and Symmetry-Breaking Charge Transfer. *Accounts of Chemical Research* **2020**, *53*, 1957–1968.
- (6) Hestand, N.; Spano, F. C. Expanded Theory of H- and J-Molecular Aggregates: The Effects of Vibronic Coupling and Intermolecular Charge Transfer. *Chemical Reviews* **2018**, *118*, 7069–7163.
- (7) Hestand, N. J.; Spano, F. C. Molecular Aggregate Photophysics beyond the Kasha Model: Novel Design Principles for Organic Materials. *Accounts of Chemical Research* **2017**, *50*, 341–350.
- (8) Spano, F. C. Symmetry-Breaking Charge Separation and Null Aggregates. *The Journal of Physical Chemistry C* **2024**, *128*, 248–260.

- (9) Bistritzer, R.; MacDonald, A. H. Moiré bands in twisted double-layer graphene. *Proceedings of the National Academy of Sciences* **2011**, *108*, 12233–12237.
- (10) Lin, C.; Kim, T.; Schultz, J. D.; Young, R. M.; Wasielewski, M. R. Accelerating symmetry-breaking charge separation in a perylenediimide trimer through a vibronically coherent dimer intermediate. *Nature Chemistry* **2022**, *14*, 786–793.
- (11) Lijina, M. P.; Benny, A.; Sebastian, E.; Hariharan, M. Keeping the chromophores crossed: evidence for null exciton splitting. *Chemical Society Reviews* **2023**, *52*, 6664–6679.
- (12) Kaufmann, C.; Bialas, D.; Stolte, M.; Würthner, F. Discrete π -Stacks of Perylene Bisimide Dyes within Folda-Dimers: Insight into Long- and Short-Range Exciton Coupling. *Journal of the American Chemical Society* **2018**, *140*, 9986–9995.
- (13) Hong, Y.; Kim, J.; Kim, W.; Kaufmann, C.; Kim, H.; Würthner, F.; Kim, D. Efficient Multiexciton State Generation in Charge-Transfer-Coupled Perylene Bisimide Dimers via Structural Control. *Journal of the American Chemical Society* **2020**, *142*, 7845–7857.
- (14) Sebastian, E.; Hariharan, M. Null Exciton-Coupled Chromophoric Dimer Exhibits Symmetry-Breaking Charge Separation. *Journal of the American Chemical Society* **2021**, *143*, 13769–13781.
- (15) Lijina, M. P.; Benny, A.; Ramakrishnan, R.; Nair, N. G.; Hariharan, M. Exciton Isolation in Cross-Pentacene Architecture. *Journal of the American Chemical Society* **2020**, *142*, 17393–17402.
- (16) Sebastian, E.; Philip, A. M.; Benny, A.; Hariharan, M. Null Exciton Splitting in Chromophoric Greek Cross (+) Aggregate. *Angewandte Chemie International Edition* **2018**, *57*, 15696–15701.

- (17) Roy, P. P.; Kundu, S.; Makri, N.; Fleming, G. R. Interference between Franck–Condon and Herzberg–Teller Terms in the Condensed-Phase Molecular Spectra of Metal-Based Tetrapyrrole Derivatives. *The Journal of Physical Chemistry Letters* **2022**, *13*, 7413–7419, PMID: 35929598.
- (18) Sahu, A.; Kurian, J. S.; Tiwari, V. Vibronic resonance is inadequately described by one-particle basis sets. *The Journal of Chemical Physics* **2020**, *153*, 224114.
- (19) Thomas, A. S.; Roy, C.; Roy, I.; Bhat, V. N.; Ghosh, S.; Tiwari, V. Disordered light-harvesting aggregates can host functional vibronic couplings at room temperature. *Nature Communications* **2026**, *17*, 3127.
- (20) Hong, Y.; Schlosser, F.; Kim, W.; Würthner, F.; Kim, D. Ultrafast Symmetry-Breaking Charge Separation in a Perylene Bisimide Dimer Enabled by Vibronic Coupling and Breakdown of Adiabaticity. *Journal of the American Chemical Society* **2022**, *144*, 15539–15548.
- (21) Kitney-Hayes, K. A.; Ferro, A. A.; Tiwari, V.; Jonas, D. M. Two-dimensional Fourier transform electronic spectroscopy at a conical intersection. *The Journal of Chemical Physics* **2014**, *140*, 124312.
- (22) Farrow, D. A.; Qian, W.; Smith, E. R.; Ferro, A. A.; Jonas, D. M. Polarized pump-probe measurements of electronic motion via a conical intersection. *The Journal of Chemical Physics* **2008**, *128*, 144510.
- (23) Förster, T. 10th Spiers Memorial Lecture. Transfer mechanisms of electronic excitation. *Discuss. Faraday Soc.* **1959**, *27*, 7–17.
- (24) Bhat, V. N.; Thomas, A. S.; Bhattacharyya, A.; Tiwari, V. Rapid scan white light pump–probe spectroscopy with 100 kHz shot-to-shot detection. *Optics Continuum* **2023**, *2*, 1981–1995.

- (25) Thomas, A. S.; Bhat, V. N.; Tiwari, V. Rapid scan white light two-dimensional electronic spectroscopy with 100 kHz shot-to-shot detection. *The Journal of Chemical Physics* **2023**, *159*, 244202.
- (26) Maret, P. D.; Sasikumar, D.; Sebastian, E.; Hariharan, M. Symmetry-Breaking Charge Separation in a Chiral Bis(peryleneimide) Probed at Ensemble and Single-Molecule Levels. *The Journal of Physical Chemistry Letters* **2023**, *14*, 8667–8675, PMID: 37733055.
- (27) Kim, S. Y.; Kim, C. H.; Park, M.; Ko, K. C.; Lee, J. Y.; Joo, T. Coherent Nuclear Wave Packets Generated by Ultrafast Intramolecular Charge-Transfer Reaction. *The Journal of Physical Chemistry Letters* **2012**, *3*, 2761–2766.
- (28) Andrzejak, M.; Skóra, T.; Petelenz, P. Is Vibrational Coherence a Byproduct of Singlet Exciton Fission? *The Journal of Physical Chemistry C* **2019**, *123*, 91–101.
- (29) Sahu, A.; Tiwari, V. Vibrations That Do Not Promote Vibronic Coupling Can Dominate Observed Lineshapes in Two-Dimensional Electronic Spectroscopy. *The Journal of Physical Chemistry Letters* **2023**, *14*, 4617–4624, PMID: 37170961.
- (30) Bhattacharyya, A.; Sahu, A.; Patra, S.; Tiwari, V. Low- and high-frequency vibrations synergistically enhance singlet exciton fission through robust vibronic resonances. *Proceedings of the National Academy of Sciences* **2023**, *120*, e2310124120.
- (31) Sahu, A.; Tiwari, V. Isolating non-adiabatically enhanced ground state quantum beats through two-dimensional electronic spectroscopy. *The Journal of Chemical Physics* **2025**, *162*, 064201.
- (32) Thomas, A. S.; Roy, C.; Roy, I.; Bhat, V. N.; Ghosh, S.; Tiwari, V. Disordered light-harvesting aggregates can host functional vibronic couplings at room temperature. *Nature Communications* **2026**, *17*, 3127.

- (33) Jonas, D. M.; Lang, M. J.; Nagasawa, Y.; Joo, T.; Fleming, G. R. Pump Probe Polarization Anisotropy Study of Femtosecond Energy Transfer within the Photosynthetic Reaction Center of Rhodobacter sphaeroides R26. *The Journal of Physical Chemistry* **1996**, *100*, 12660–12673.
- (34) Wega, J.; Rumble, C. A.; Vauthey, E. Ground-State Structure and Excited-State Dynamics of a Donor–Acceptor Complex with Two Charge-Transfer Bands. *The Journal of Physical Chemistry Letters* **2025**, *16*, 5327–5333, PMID: 40394870.
- (35) Markovic, V.; Villamaina, D.; Barabanov, I.; Lawson Daku, L. M.; Vauthey, E. Photoinduced Symmetry-Breaking Charge Separation: The Direction of the Charge Transfer. *Angewandte Chemie International Edition* **2011**, *50*, 7596–7598.
- (36) Qian, W.; Jonas, D. M. Role of cyclic sets of transition dipoles in the pump–probe polarization anisotropy: Application to square symmetric molecules and perpendicular chromophore pairs. *The Journal of Chemical Physics* **2003**, *119*, 1611–1622.
- (37) Smith, E. R.; Jonas, D. M. Alignment, Vibronic Level Splitting, and Coherent Coupling Effects on the Pump-Probe Polarization Anisotropy. *The Journal of Physical Chemistry A* **2011**, *115*, 4101–4113, PMID: 21417384.
- (38) Halasinski, T. M.; Weisman, J. L.; Ruiterkamp, R.; Lee, T. J.; Salama, F.; Head-Gordon, M. Electronic Absorption Spectra of Neutral Perylene (C₂₀H₁₂), Terrylene (C₃₀H₁₆), and Quaterrylene (C₄₀H₂₀) and Their Positive and Negative Ions: Ne Matrix-Isolation Spectroscopy and Time-Dependent Density Functional Theory Calculations. *The Journal of Physical Chemistry A* **2003**, *107*, 3660–3669.
- (39) Tiwari, V.; Peters, W. K.; Jonas, D. M. Electronic resonance with anticorrelated pigment vibrations drives photosynthetic energy transfer outside the adiabatic framework. *Proceedings of the National Academy of Sciences* **2013**, *110*, 1203–1208.

- (40) Kistler, K. A.; Spano, F. C.; Matsika, S. A Benchmark of Excitonic Couplings Derived from Atomic Transition Charges. *The Journal of Physical Chemistry B* **2013**, *117*, 2032–2044, PMID: 23391106.
- (41) Tiwari, V.; Peters, W. K.; Jonas, D. M. Electronic energy transfer through non-adiabatic vibrational-electronic resonance. I. Theory for a dimer. *The Journal of Chemical Physics* **2017**, *147*, 154308.
- (42) Tiwari, V.; Jonas, D. M. Electronic energy transfer through non-adiabatic vibrational-electronic resonance. II. 1D spectra for a dimer. *The Journal of Chemical Physics* **2018**, *148*, 84308.
- (43) Womick, J. M.; Moran, A. M. Vibronic Enhancement of Exciton Sizes and Energy Transport in Photosynthetic Complexes. *J. Phys. Chem. B* **2011**, *115*, 1347–1356.
- (44) Witkowski, A.; Moffitt, W. Electronic Spectra of Dimers: Derivation of the Fundamental Vibronic Equation. *The Journal of Chemical Physics* **1960**, *33*, 872–875.
- (45) Jonas, D. M. Vibrational and Nonadiabatic Coherence in 2D Electronic Spectroscopy, the Jahn–Teller Effect, and Energy Transfer. *Annual Review of Physical Chemistry* **2018**, *69*, 327–352.
- (46) Snellenburg, J. J.; Liptonok, S.; Seger, R.; Mullen, K. M.; van Stokkum, I. H. M. Glotaran: A Java-Based Graphical User Interface for the R Package TIMP. *Journal of Statistical Software* **2012**, *49*, 1–22.

Acknowledgements

S.P. and S.G. acknowledge the research fellowship from IISc Bangalore. A.B. acknowledges the Prime Minister’s Research Fellowship, MoE, India. V.N.B. acknowledges the DST-Inspire research scholarship.

J.S. acknowledges the University Grants Commission (UGC) for financial support. P.D.M thanks IISER TVM for financial assistance. M.H. acknowledges MoE-STARS/STARS-2/2023-0770 for financial support.

Author Contributions

V.T. and M.H. conceptualized the project. S.P. optimized and performed the pump-probe and anisotropy experiments with help from V.N.B., A.B. and S.G. J.S. carried out the synthesis of SpPDI2 and performed the electronic structure calculations. P.D.M performed the synthesis and electronic structure calculations for the chiral CyPDI2 dimer. S.P. performed the vibronic exciton model calculations. V.T. wrote the manuscript with contributions from S.P. All authors discussed the results and commented on the manuscript.

Competing Interests

The authors declare no competing interests.